Prediction of two-dimensional bismuth-based chalcogenides Bi_2X_3(X = S, Se, Te) monolayers with orthorhombic structure : a first-principles study

Prediction of Two Dimensional bismuth-based chalcogenides Bi_2X_3 (X=S, Se, Te) monolayers with orthorhombic structure: A First-principles study

A. Bafekry,[1,2,*] M. Faraji,[3] M. M. Fadlallah,[4] H. R. Jappor,[5]
N. N. Hieu,[6,7] M. Ghergherehchi,[8] S.A.H. Feghhi,[1] and D. Gogova[9]

[1]*Department of Radiation Application, Shahid Beheshti University, Tehran, Iran*
[2]*Department of Physics, University of Antwerp, Groenenborgerlaan 171, B-2020 Antwerp, Belgium*
[3]*Micro and Nanotechnology Graduate Program, TOBB University of Economics and Technology, Sogutozu Caddesi No 43 Sogutozu, 06560, Ankara, Turkey*
[4]*Department of Physics, Faculty of Science, Benha University, 13518 Benha, Egypt*
[5]*Department of Physics, College of Education for Pure Sciences, University of Babylon, Hilla, Iraq*
[6]*Institute of Research and Development, Duy Tan University, Da Nang 550000, Viet Nam*
[7]*Faculty of Natural Sciences, Duy Tan University, Da Nang 550000, Viet Nam*
[8]*Department of Electrical and Computer Engineering, Sungkyunkwan University, 16419 Suwon, Korea*
[9]*Department of Physics, University of Oslo, P.O. Box 1048, Blindern, Oslo, Norway*

First-principles calculation is a very powerful tool for discovery and design of novel two-dimensional materials with unique properties needed for the next generation technology. Motivated by the successful preparation of Bi_2S_3 nanosheets with orthorhombic structure in the last year [K. A. Messalea et al., Adv. Mater. Interfaces 7, 2001131 (2020)] herein we gain a deep theoretical insight into the crystal structure, stability, electronic and optical properties of Bi_2X_3 (X=S, Se, Te) monolayers of orthorhombic phase employing the first-principles calculations. The Molecular dynamics study, phonon spectra, criteria for elastic stability, and cohesive energy results confirm the desired stability of the Bi_2X_3 monolayers. From S, to Se and Te, the work function value as well as stability of the systems decrease due to the decline in electronegativity. Mechanical properties study reveals that Bi_2X_3 monolayers have brittle nature. The electronic bandgap values of Bi_2S_3, Bi_2Se_3 and Bi_2Te_3 monolayers are predicted by the HSE06 functional to be 2.05 eV, 1.20 eV and 1.16 eV, respectively. By assessing the optical properties, it has been found that Bi_2X_3 monolayers can absorb ultraviolet light. The high in-plane optical anisotropy offers an additional degree of freedom in the design of optical devices. The properties revealed in our survey will stimulate and inspire the search for new approaches of orthorhombic Bi_2X_3 (X=S, Se, Te) monolayers synthesis and properties manipulation for fabrication of novel nanoelectronic and optoelectronic devices.

I. INTRODUCTION

The bismuth-based chalcogenide compounds, particularly, Bi_2S_3, Bi_2Se_3 and Bi_2Te_3 have gained special interest due to their unrivalled electronic, thermoelectric and optical properties, such as low thermal conductivity, large Seebeck coefficients, small effective carrier masses, and thickness-dependent bandgap.[1–3] Therefore, bismuth chalcogenide compounds are suitable for a wide variety of applications including thermoelectric energy conversion,[4] spintronics,[5] infrared photography,[6] photosensitive and optical devices.[7] Moreover, due to the feature of intralayer anisotropic crystal structures, the bismuth-based chalcogenide nanomaterials exhibit direction-dependent optical, thermal, electronic properties such as the transport of charge in different crystal axes, which can be profitable for invention of innovative devices like direction-sensitive sensors and high-speed optoelectronic devices.[8] Besides, the anisotropic feature often causes the optical excitation to become strongly dependent on polarization. In addition to peculiar quantum effects by heavy spin-orbit coupling including novel phenomena related to spin[9] and the irregular quantum Hall effect.[10]

The Bi_2S_3 has drawn considerable attention and has been extensively used for electrochemical hydrogen production,[11] thermoelectrics,[12] photodetectors,[13] X-ray tomography imaging,[14] sensing and memory switching devices.[15] This large interest is due to the materials optimal bandgap (1.3-2.3 eV),[16] strong spin-orbit coupling,[17] absorption coefficient (105 cm^{-1}),[18] highly anisotropic structure,[19] and good thermoelectric properties.[20] Similarly, Bi_2Se_3 belongs to the class of transition metal trichalcogenides and it has received prodigious attention to be exploited in thermoelectrics[21] and low-energy electronics.[22] Bi_2Se_3 is a semiconductor with an energy bandgap in the range of 0.24 -0.35 eV according to the experimental measurements and theoretical calculations.[3] At the Γ point, Bi_2Se_3 has a basic and robust surface state.[23] Even though the bulk of this material possesses a relatively large semiconductor bandgap, the electrical measurements disclosed that its charge transport features may differ considerably depending on the sample preparation conditions,[24] with a significantly high inclination for the bulk Bi_2Se_3 as an n-type semiconductor,[25] due to native n-type defects such as excess of Se or atomic vacancies.

Equally important, Bi_2Te_3 has gathered great attention in physics and material science[26,27] because of its exotic electromagnetic phenomena including the magnetic monopoles and superconducting proximity effect. Similar to Bi_2Se_3, the Bi_2Te_3 shows a strong spin-orbit induced indirect bulk energy gap semiconductor.[28]

Generally, electron donors control the electrical properties of crystal Bi_2Te_3, leading to n-type conductivity. On the other hand, two dimensional (2D) materials, have attracted considerable attention due to their exceptional properties such as tunable optoelectronic properties, good mechanical properties, superior electron carrier mobility, good gas sensing, high surface-volume ratio, etc.[29–36] Meanwhile, the thermoelectric efficiency, electrochemical and photoresponse properties of a number of 2D materials were estimated first theoretically.[37] Among these 2D materials, Bi_2X_3 (X= S, Se, Te) monolayers show interesting properties and thus can be used in spintronic devices,[38] construction of high-performance thermoelectric devices,[39] supercapacitors,[40] and nanoscale photodetectors.[41] Astoundingly, Bi_2X_3 (X= S, Se, Te) in their both forms (2D and bulk) were studied experimentally by ARPES[23] and synthesized by molecular-beam epitaxy,[42] green ionothermal synthesis,[43] photoelectron spectroscopy,[44] unidirectional solidification,[45] hydrothermal growth),[46] solvothermal synthesis,[47] chemical vapor deposition,[48] high-power sonication process,[49] and consecutive epitaxial growth of nanoplates[22] methods. The discussion above confirm that Bi_2X_3(X= S, Se, Te) can be effectively used as prospective materials in different applications.

Remarkably, very recently the orthorhombic 2D Bi_2S_3 nanosheets have been synthesized using a novel liquid-metal-based fabrication method.[50] The 2D nanosheets with a highly anisotropic orthorhombic crystal structure have demonstrated outstanding electronic properties including a high hole mobility of 28 $cm^2V^{-1}s^{-1}$, high photoresponsivity (8 A/W), with intraplane van der Waals gaps and a direct bandgap value of 2.3 eV.[50] Although the hexagonal Bi_2X_3(X= S, Se, Te) monolayers have been elaborated and explored over the past decade as excellent thermoelectric materials, the physical properties of the novel orthorhombic Bi_2X_3(X= S, Se, Te) monolayers remain unexplored.

In view of the foregoing, the purpose of the present work is to gain a deeper insight into the stability, mechanical, electronic, and optical properties of the novel 2D Bi_2X_3 (X=S, Se, Te) monolayers crystallized in orthorhombic structure by exploiting the powerful density functional theory (DFT). 2DMs with high in-plane anisotropy, like the considered here, provide an additional degree of freedom in device design. The properties revealed by our investigations will stimulate and expire the search for new approaches of orthorhombic Bi_2X_3 (X=S, Se, Te) monolayers synthesis and properties manipulation for fabrication of novel nanoelectronic and optoelectronic devices.

II. METHOD

In this paper, we perform DFT calculations as implemented in the Vienna ab-initio Simulation Package (VASP).[53,54] The projector augmented wave (PAW) method and the generalized gradient approximation (GGA) with the Perdew-Burke-Ernzerhof (PBE) functional[51,52] have been employed in the computations. The kinetic energy cut-off of 500 eV was set for plane-wave expansion and the atomic structures of investigated systems were relaxed until fluctuations in the energies and total Hellmann-Feynman forces fall below 10^{-8} eV and 10^{-7} eV/Å, respectively. Convergence using the $21 \times 21 \times 1$ k-points was achieved for the primitive unit cell. To avoid the image interaction, the vacuum space was 20 Å along the z-axis. We calculated the phonon spectra of systems using the small displacement method via the PHONOPY package.[59] The $(2 \times 2 \times 1)$ supercells with $(2 \times 2 \times 1)$ k-points were built for the ab-initio molecular dynamics (AIMD) simulations. The AIMD simulations were performed at 400 K with 1000 time-steps for each calculation. We chose half the AIMD trajectories to built the training sets. The band structures were calculated using the PBE, PBE plus spin-orbit coupling (PBE+SOC), and the Heyd-Scuseria-Ernzerhof (HSE06)[55] functionals to get more accurate estimation of the bandgaps. We used the Bader charge analysis[57] to describe the charge transfer in the systems investigated. The DFT-D3 method by Grimme[58] was also employed to consider the long-range attractive van der Waals forces in the systems. The optical characteristics were calculated in the random phase approximation using the PBE functional. The absorption coefficient $\alpha(\omega)$ and refractive index $n(\omega)$ were evaluated by:

$$\alpha(\omega) = \sqrt{2}\omega\sqrt{\sqrt{\varepsilon_1^2(\omega) + \varepsilon_2^2(\omega)} - \varepsilon_1(\omega)}, \tag{1}$$

and

$$n(\omega) = \frac{1}{\sqrt{2}}(\sqrt{\varepsilon_1^2(\omega) + \varepsilon_2^2} + \varepsilon_1(\omega))^{1/2}, \tag{2}$$

where $\varepsilon_1(\omega)$ and $\varepsilon_2(\omega)$ refer respectively to the real and imaginary parts of the dielectric function at incoming light frequency ω, which can be written as:

$$\varepsilon_2(\omega) = \frac{(2\pi e)^2}{(m\omega)^2 V} \sum_{k,i} \langle \psi_k^v | p_i | \psi_k^c \rangle \delta(E_{\psi_k^c} - E_{\psi_k^v} - \hbar\omega), \tag{3}$$

and

$$\varepsilon_1(\omega) = \frac{2}{\pi} P \int d\omega' \, \frac{\varepsilon_2(\omega')}{\omega' - \omega}, \tag{4}$$

where e, m, V, p, and P are the charge, mass of the electron, the volume of the supercell, momentum operator, and the Cauchy principal value, respectively. The $E_{\psi_k^v}$, $E_{\psi_k^c}$, and $\hbar\omega$ are the occupied, unoccupied, and incident light energies, correspondingy.

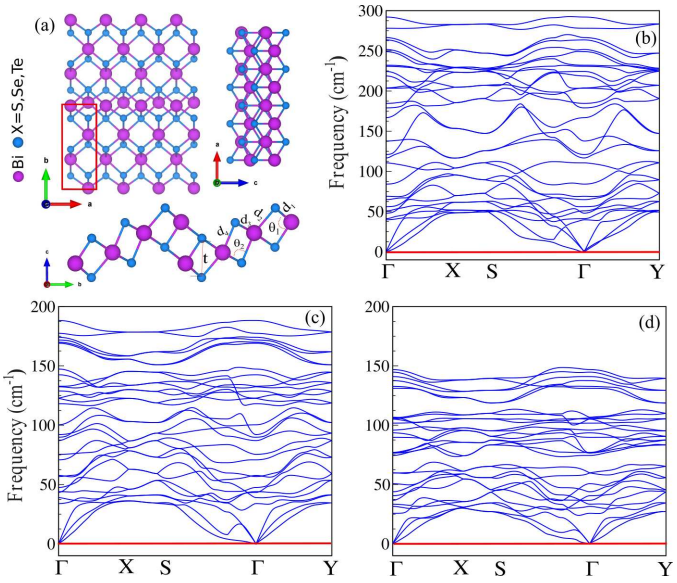

Figure 1. (a) The structures of Bi_2X_3 (X=S, Se, Te) monolayers (the side view shows the structural parameters). Phonon spectrum of the (b) Bi_2S_3, (c) Bi_2Se_3 and (d) Bi_2Te_3 monolayer. The primitive cell is pointed out by a red rectangle.

III. STRUCTURAL PROPERTIES

The top and side views of the atomic structures of Bi_2X_3 (X=S, Se, Te) monolayers with an orthorhombic lattice are displayed in 1(a). The primitive unit cell of the Bi_2X_3 belongs to the space group *Pmcn* and is formed by 10 atoms (4 Bi and 6 X) and indicated by a red rectangle. In the crystal structure of Bi_2X_3 (X=S, Se, and Te), each X atom is encompassed by four Bi atoms, and each Bi atom is encircled by six X atoms. Notice, $\vec{\mathbf{a}}$ and $\vec{\mathbf{b}}$ ($\vec{\mathbf{a}} \neq \vec{\mathbf{b}}$) are the translational vectors. The lattice constants of a (b) of the Bi_2S_3, Bi_2Se_3 and Bi_2Te_3 monolayers are determined to be: 4.02 (9.02) Å, 4.11 (9.98) Å and 4.30 (10.38) Å, respectively. A schematic view of the structural parameters in the Bi_2X_3 lattice is presented in Fig. 1(a). We found out that the bond lengths $d_{1,2}$ ($d_{3,4}$) are: 3.00 Å, 2.76 Å (2.82 Å, 2.97 Å), respectively for the Bi_2S_3, while for the Bi_2Se_3 are 2.82 Å, 2.97 Å (2.84 Å, 2.93 Å) and in the case of Bi_2Te_3 are 3.01 Å, 3.13 Å (3.02 Å,3.12 Å).

The two angles of X-Bi-X are calculated to be 90 °, 78° (Bi_2S_3), 94 °, 81° (Bi_2Se_3) and 96 °, 81° (Bi_2Te_3). Notice, the considered monolayers have highly anisotropic lattices. The thickness of Bi_2S_3, Bi_2Se_3 and Bi_2Te_3 monolayers are calculated to be 3.15 Å, 3.64 Å and 4.04 Å, respectively. The structural parameters are collected in Tabel I. The Bi-X average bond lengths, X–Bi–X angle and the thicknesses increase with the rise of the X atom size, where the atomic radii of S, Se, and Te are 105 pm, 120 pm, and 138 pm, correspondingly.

The cohesive energy per atom E_{coh} can be estimated as:

$$E_{coh} = \frac{E_{tot} - 6E_X - 4E_{Bi}}{10}, \tag{5}$$

where E_X and E_{Bi} represent the energies of isolated single X and Bi atoms, respectively. Ten is the number of atoms in the unit cell, E_{tot} stands for the total energy of the Bi_2X_3 monolayer. The cohesive energy of Bi_2S_3, Bi_2Se_3, and Bi_2Te_3 are found to be −8.08 eV/atom, −7.50 eV/atom, and −6.81 eV/atom, respectively. The results obtained demonstrate that Bi_2X_3 monolayers are stable structures and the Bi_2S_3 is the most stable within the monolayers considered due to the higher electronegativity of S (2.58) in comperison to that of Se (2.55) and Te (2.10).

IV. DYNAMICAL AND THERMAL STABILITY

The dynamical stability is investigated by means of analysis of the phonon spectra, which are illustrated in Figs. 1(b-d). Apparently, the phonon branches do not have imaginary modes (negative values) confirming the dynamical stability of the structures studied. Next we assess the stability of Bi_2X_3 via calculating their phonon spectra as well as by AIMD simulations at 400 K. The temperature fluctuation and the optimized structures after 5 ps of simulation of the Bi_2X_3 monolayers, calculated by the AIMD, are indicated in Figs. 2(a) and (b), respectively. Our AIMD simulations demonstrate the Bi_2X_3 structures are still robust and no structural reconstruction is observed after heating at 400 K, implying that the Bi_2X_3 monolayers are thermally stable.

The electron localization functions (ELF) of the Bi_2X_3 monolayers are illustrated in Fig. 2(c). The blue/red region refers to the low/high electron density of Bi_2S_3, Bi_2Se_3, and Bi_2Te_3. The difference charge density ($\Delta\rho$) is defined as: $\Delta\rho = \rho_{tot} - \rho_X - \rho_{Bi}$, where ρ_{tot} and $\rho_{X/Bi}$ are the charge densities of the Bi_2X_3 and isolated X/Bi atoms. The computational results demonstrate that there is a charge transfer from Bi to X atoms in Bi_2X_3 with the corresponding charge amount of $0.82e$, $0.60e$, and $0.44e$ for X= S, Se, and Te, accordingly. The Bi ions are positively charged and surround the negatively charged S, Se and Te ions. Worthy to note that the charge redistribution originates from the different electronegativities of Bi (2.02), S (2.58), Se (2.55) and Te (2.10). The charge transfer of Bi_2X_3 decreases with the electronegativity decline of the corresponding X atom.

V. MECHANICAL PROPERTIES

We also examine the mechanical stability of Bi_2X_3 monolayers via calculations of their elastic constants. In the framework of the harmonic approximation, Bi_2X_3 monolayer has thirteen independent elastic constants due

Table I. Electronegativity χ of X atom, calculated lattice constants a, b, Bi–X bond length d, X–Bi–X bond angle $\theta_{1,2}$, thickness t, cohesive energy E_{coh}, charge transfer ΔQ, work function Φ, bandgap (E_g) using the PBE (PBE+SOC) of Bi_2X_3 (X=S, Se, Te) monolayers.

	χ	$a(b)$ (Å)	d (Å)	t (Å)	$\theta_{1,2}$ (°)	E_{coh} (Å)	ΔQ (eV/atom)	Φ (e)	E_g (eV)
Bi_2S_3	2.58	4.02 (9.02)	2.88	3.15	90, 78	-8.08	0.82	5.72	1.50 (0.95)
Bi_2Se_3	2.56	4.11 (9.98)	2.89	3.64	94, 81	-7.50	0.60	5.42	1.20 (0.75)
Bi_2Te_3	2.10	4.30 (10.38)	3.07	4.04	96, 81	-6.81	0.44	4.03	1.10 (0.45)

Table II. The elastic constant parameters (GPa), bulk modulus B (GPa), shear modulus S (GPa), Young's modulus Y (GPa), Poisson's ratio ν), and bulk/shear ratio B/S of Bi_2X_3 (X=S, Se, Te) monolayers.

	C_{11}	C_{12}	C_{13}	C_{22}	C_{23}	C_{33}	C_{44}	C_{55}	C_{66}	B	S	Y	ν	B/S
Bi_2S_3	25.49	1.45	0.32	2.32	0.27	1.42	8.97	0.43	0.48	3.70	3.79	8.48	0.12	0.98
Bi_2Se_3	24.91	3.26	0.38	6.55	0.32	1.6	9.03	0.52	0.53	4.56	3.96	9.21	0.16	1.15
Bi_2Te_3	20.39	3.67	0.06	6.83	0.03	0.43	7.66	0.08	0.10	3.91	3.17	7.47	0.18	1.23

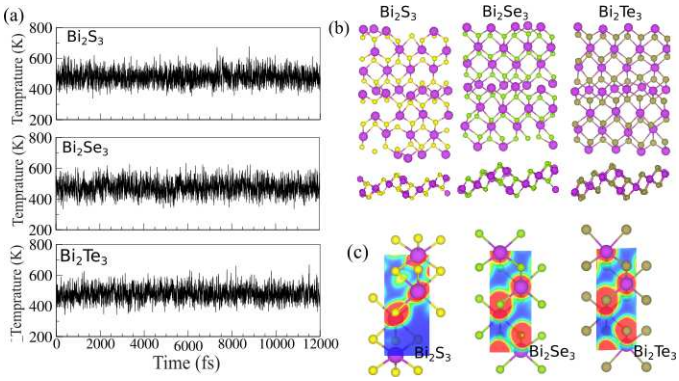

Figure 2. (a) Temperature fluctuation, (b) optimized structure after 5 ps of simulation and (c) contour plot of the electron localization function (ELF) of the Bi_2X_3 (X=S, Se, Te) monolayers. Red (blue) color indicates high (low) electron density.

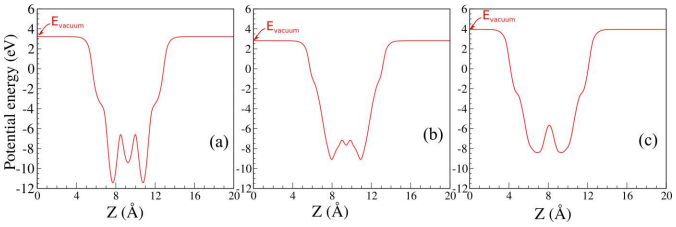

Figure 3. Electrostatic potential of the (a) Bi_2S_3, (b) Bi_2Se_3 and (c) Bi_2Te_3 monolayers.

to its $P2_1/m$ space group, leading to anisotropic mechanical properties. The Bi_2X_3 structures verify the twelve elastic stability criteria.[61] The elastic constants (given in Table II) are used to calculate the bulk modulus (B), shear modulus (S), bulk/shear ratio (BS), Young's modulus (Y), and Poisson's ratio (ν) by means of the Voigt Reuss-Hill method[60] (summarized in Table II). Our calculations reveal the bulk modulus of B of Bi_2S_3, Bi_2Se_3, and Bi_2Te_3 are 3.70, 4.55 and 3.91 GPa, accordingly. Therefore, the Bi_2Se_3 monolayer can resist larger compressive strain than its counterparts - Bi_2Se_3 and Bi_2Te_3. We have also confirmed these results via calculations of the Young's moduli, which are listed in Table II. The Young's moduli of Bi_2S_3, Bi_2Se_3, and Bi_2Te_3 are 8.48, 9.21 and 7.47 GPa, respectively. The shear modulus S refers to the resistance to the change in the shape of materials, where S increases as the rigidity of the structure increases too. The shear moduli are determined 3.79 GPa (Bi_2S_3), 3.96 GPa (Bi_2Se_3) and 3.17 GPa (Bi_2Te_3), which indicate Bi_2Se_3 is the most rigid in comparison to Bi_2S_3 and Bi_2Te_3. The B/S ratio refers to the brittle/ductile nature of the materials. Notice that, the B/S ratio in Bi_2X_3 increases as the X atoms move down from S to Te being 0.98, 1.15, 1.23 for Bi_2S_3, Bi_2Se_3, and Bi_2Te_3, respectively. This implies that all Bi_2X_3 structures possess brittle nature because their B/S ratios are smaller than 1.75.[62] Also, the Poissons's ratio P calculations confirm the brittle nature of the Bi_2X_3 structures. The computations indicate the Poissons's ratio are calculated 0.12 (Bi_2S_3), 0.16 (Bi_2Se_3) and 0.18 (Bi_2Te_3), which are smaller than 0.33[63]

Further, we study other fundamental quantity, the electrostatic potential of the Bi_2X_3 monolayers. The computational results are illustrated in Figs. 3(a-c). Obviously, the electrostatic potentials of the Bi_2X_3 monolayers are flat in the vacuum region. As the electronegativity increases the depth of the electrostatic potential increases too. The work function can be estimated as $\Phi = E_{vacuum} - E_F$, where E_{vacuum} is the energy of the vacuum, that is extracted from the electrostatic potential (see Figs. 3(a-c)), and E_F is the Fermi energy. The work function values of the Bi_2S_3, Bi_2Se_3 and Bi_2Te_3 monolayers are calculated to be: 5.72, 5.42 and 4.03 eV, re-

spectively. Apparently, the work function decreases with the electronegativity decline of the X atom.

VI. ELECTRONIC PROPERTIES

The electronic band structures of Bi_2X_3 monolayers calculated within the PBE functional are displayed in Figs. 4(a-c). At the ground state, Bi_2S_3 is a semiconductor with an indirect bandgap of 1.50 eV. As manifasted in Fig. 4, the valence band minimum (VBM) lies on the ΓX path, while the conduction band maximum (CBM) is at the Y-point. Similar to Bi_2S_3, the Bi_2Se_3 and Bi_2Te_3 exhibit semiconducting characteristics with indirect bandgaps of 1.20 eV and 1.10 eV, respectively. It is noted that the PBE functional typically underestimates the semiconductor bandgap value. Therefore, the HSE06 functional has also been used to study the electronic band structures. Evidently, the band structures calculated by the HSE06 (Fig. 4(a-c)), red bands) and the PBE/GGA functionals are very similar. The indirect bandgaps of Bi_2S_3, Bi_2Se_3 and Bi_2Te_3 increase to 2.05 eV, 1.20 eV, and 1.16 eV, respectively, as compared to the corresponding values determined by the PBE and PBE+SOC calculations. The HSE06 effect shifts the CB as a whole to higher energies (relative to the Fermi energy), while the VB remains rigid. The effects of spin-orbital coupling (SOC) on the electronic band structures of Bi_2X_3 monolayers are shown in Fig. 4(d) (red bands). The bandgap values of the monolayers studied decrease to 0.95 eV (Bi_2S_3), 0.75 eV (Bi_2Se_3) and 0.45eV (Bi_2Te_3) as compared to the corresponding values determined by the PBE calculations. The SOC effect shifts the CB as a whole to the lower energies (relative to the Fermi energy), while the VB remains rigid.

The density of states (DOS) of Bi_2X_3 structures are depicted in Figs. 4(a-c). It is obvious the semiconducting character of Bi_2X_3 comes from the S-, Se- and Te-states in the VBM, while Bi-states dominate in the CBM. In order to explain the origin of the electronic states, the projected densities of states (PDOS) of Bi_2X_3 are shown in Fig. 5(a). From PDOS, the VBM is composed of the p_z and $p_{x,y}$ of S atoms, while the CBM arises from the p_z and $p_{x,y}$ states of S- and Bi-atoms. We discover the VBM of Bi_2Se_3 and Bi_2Te_3 originates from the Se/Te-$p_{x,y}$ states, while the CBM consists of Se/Te-p_z and Bi-p_z states. The charge densities of the CBM and VBM orbitals of Bi_2X_3 are exhibited in Figs. 5(b). However, while in the Bi_2S_3, Bi_2Se_3 monolayers, the holes and electrons are mainly distributed in the plane of the S and Se atoms and overlapped together, in the Bi_2Te_3 monolayer, the holes and electrons are distributed on the Te and Bi atoms, which agrees with the PDOS of Bi_2X_3 monolayers. Meanwhile, the excited electrons mainly rise around the chalcogenide atoms, and consequently, the holes and electrons separation in the Bi_2X_3 monolayers is distinctive.

VII. OPTICAL PROPERTIES

To uncover the optical properties of the orthorombic Bi_2X_3 monolayers we have calculated their dielectric constants and the results are depicted in Figs. 6(a,b). Our calculations indicate that the optical characteristics of Bi_2X_3 along x and y directions are very similar. Every real dielectric constant has two peaks for every component, Fig. 6(a), the first peak locates below 6 eV and the second peak is positioned above 8 eV. The first peak is located at 4.8 eV for all Bi_2X_3 structures for the x component, while it is positioned at 5.0 eV for Bi_2S_3

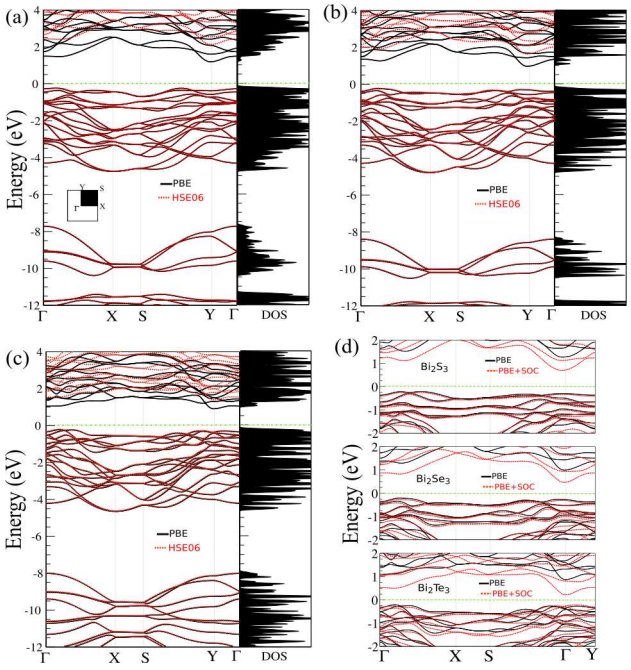

Figure 4. Band structure and DOS using PBE and HSE06 of the (a) Bi_2S_3, (b) Bi_2Se_3, (c) Bi_2Te_3 monolayer, and (d) Band structure using PBE and (PBE+SOC) of the Bi_2X_3 (X=S, Se, Te) monolayers. The Fermi level is set at zero.

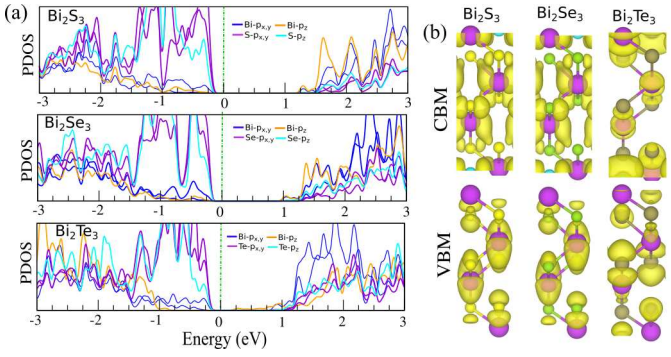

Figure 5. (a) Projected density of states and (b) charge densities of the CBM and VBM orbitals of (a) Bi_2S_3, (b) Bi_2Se_3 and (c) Bi_2Te_3 monolayer. The zero of energy is set to the Fermi level.

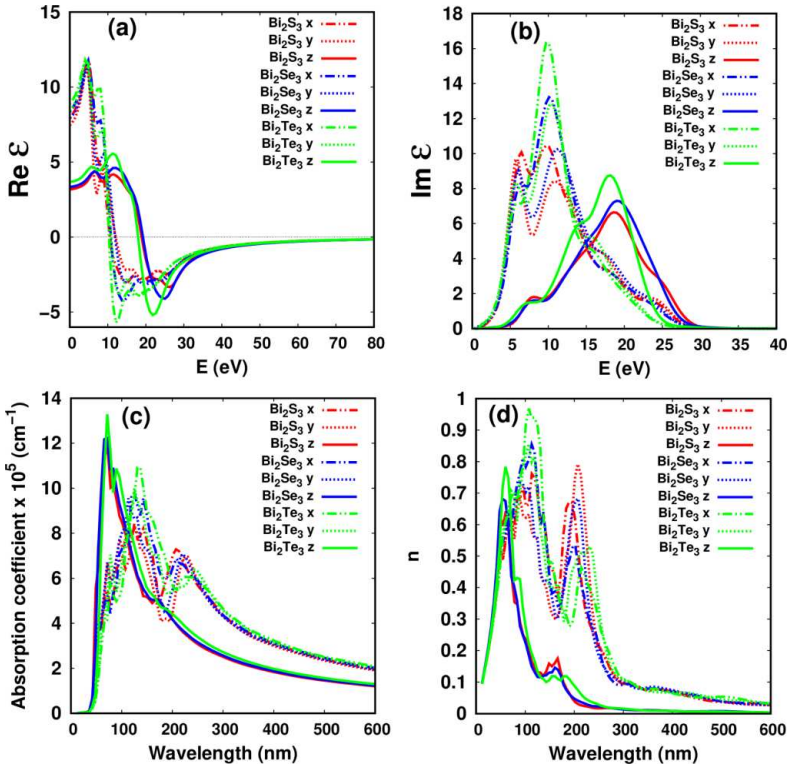

Figure 6. (a) Real and (b) imaginary parts of the dielectric constant. (c) Absorption coefficient (d) refractive index of Bi_2X_3 monolayers for x, y and z components.

and Bi_2Se_3, and at 4.5 eV for Bi_2Te_3 with respect to y component. Regarding the z component, the first peak appears at 6.0 for Bi_2S_3 and Bi_2Se_3, and at 5.4 eV for Bi_2Te_3. For the imaginary part of the dielectric constant (Fig. 6(b)), the starting points of the x and y components is related to the bandgaps of Bi_2X_3 monolayers. Similar to the real part, there are two peaks for every component. The first peak locates below 7.0 eV and the second peak is situated above 9.0 eV. For x component the first peak locates at 6.5, 6.3, 5.5 for X=S, Se, and Te, respectively. While for the y component it locates at 6.0 eV, 6.1 eV and 5.8 eV for X=S, Se, and Te, accordingly. For the last component, z, the first peak locates at 8.0 eV for all structures. The z component peaks locate at a higher energy as compared to the x and y components in the same structures for both real and imaginary dielectric constants. The imaginary part peaks locate at higher energy as compared to the corresponding real part peaks. The static dielectric constants $\varepsilon_1(0)$ are 0.8 for x and y directions of X=S and Se and 0.9 for X=Te. While they are 0.3 for x and y components of X=S and Se and 0.4 for X=Te.

Turning to the absorption spectra, Fig. 6(c) exhibits the absorption coefficients of the orthorombic Bi_2X_3 monolayers as a function of wavelength. All components have an absorption peak at 80 nm and there are other two peaks at 140 nm and 240 nm for the x and y directions, respectively. The positions of the absorption peaks indicate that Bi_2X_3 structures are active in the ultraviolet spectral region. The absorption peak positions are consistent with the dielectric constant peak positions. Fig. 6(d) depicts the refractive index dispersion of Bi_2X_3. Obvioulsy, the behavior of the refractive index is similar to the behavior of the absorption coefficient. The static refractive index for all Bi_2X_3 is 0.1. The refractive indexes have maximum values at 100 nm in x direction, which are 0.75, 0.85 and 0.98 for X=S, Se, and Te, respectively. In the visible region (600 nm), the refractive indexes for all structures are very small $\sim$ 0.02 for x and y direction.

VIII. CONCLUSION

Novel Bi_2X_3 (X=S, Se, Te) monolayer structures of orthorhombic crystallographic phase are introduced. The stability, electronic, and optical properties are investigated in detail by first principle calculations. The stability examinations are confirmed by phonon dispersion study, the dynamical and thermal regimes including molecular dynamics, cohesive energy, and elastic stability criteria calculations. The mechanical properties exploration shows Bi_2X_3 have brittle nature. We discover the Bi_2Se_3 monolayer can resist to compression more than its counterparts. The cohesive energy per atom, the amount of transferred charge, and the work function of Bi_2X_3 structures decrease as we move from S to Se and Te,

which is related to the electronegativity decline. Meanwhile, the Bi-X distance, the bond angle between X-Bi-X, and the thickness increase from S to Se and Te due to the atomic size increase. All structures considered are indirect bandgap semiconductors. Using the PBE (HSE06) method the bandgap values of Bi_2S_3, Bi_2Se_3 and Bi_2Te_3 orthorhombic monolayers are predicted to be 1.12 (2.05) eV, 0.81 (1.20) eV and 0.75 (1.26) eV, respectively. The spin-orbit coupling effect decreases the bandgaps. The orthorhombic Bi_2X_3 monolayers can be active in the ultraviolet spectral region. Our survey confirms the stability and highlights the outstanding prospects of the Bi_2X_3 (Bi_2S_3, Bi_2Se_3 and Bi_2Te_3) orthorhombic nanosheets in nanoelectronic and optoelectronic applications utilizing the high in-plane anisotropy.

IX. DECLARATION OF COMPETING INTEREST

The authors declare that they have no known competing financial interests or personal relationships that could have appeared to influence the results reported in this paper.

X. ACKNOWLEDGMENTS

This work was supported by the National Research Foundation of Korea grant funded by the Korea Government (MSIT) (NRF-2015M2B2A4033123).

* bafekry.asad@gmail.com

[1] L.B. Zhan, C.L. Yang, M.S. Wang, X.G. Ma, Phys. E Low-Dimensional Syst. Nanostructures. 124 (2020) 114272.
[2] Z. Rashid, A.S. Nissimagoudar, W. Li, Phys. Chem. Chem. Phys. 21 (2019) 5679-5688.
[3] S.K. Mishra, S. Satpathy, O. Jepsen, J. Phys. Condens. Matter. 9 (1997) 461-470.
[4] P. Ghaemi, R.S.K. Mong, J.E. Moore, Phys. Rev. Lett. 105 (2010) 166603.
[5] J.E. Moore, Nat. 464 (2010) 194-198.
[6] R.N. Bhattacharya, P. Pramanik, J. Electrochem. Soc. 129 (1982) 332-335.
[7] C.W. Bates, L. England, Appl. Phys. Lett. 14 (1969) 390-392.
[8] Y. Liu, Y. Xu, Y. Ji, H. Zhang, Phys. Chem. Chem. Phys. 22 (2020) 9685-9692.
[9] Y. Okada, C. Dhital, W. Zhou, E.D. Huemiller, H. Lin, S. Basak, A. Bansil, Y.B. Huang, H. Ding, Z. Wang, S.D. Wilson, V. Madhavan, Phys. Rev. Lett. 106 (2011) 206805.
[10] R. Yu, W. Zhang, H.J. Zhang, S.C. Zhang, X. Dai, Z. Fang, Sci. 329 (2010) 61-64.
[11] A. Li, N. Sun, Y. Huang, Y. Qin, N. Zhao, J. Gao, M. Li, H. Zhou, L. Qi, Adv. Funct. Mater. 18 (2008) 1194-1201.
[12] S.C. Liufu, L.D. Chen, Q. Yao, C.F. Wang, Appl. Phys. Lett. 90 (2007) 112106.
[13] G. Konstantatos, L. Levina, J. Tang, E.H. Nano Lett. 8 (2008) 4002-4006.
[14] O. Rabin, J.M. Perez, J. Grimm, G. Wojtkiewicz, R. Weissleder, Nat. Mater. 5 (2006) 118-122.
[15] S.K. Das, P. Padhan, ACS Appl. Nano Mater. 3 (2020) 274-282.
[16] H. Kim, C. Jin, S. Park, W.I. Lee, I.J. Chin, C. Lee, Chem. Eng. J. 215-216 (2013) 151-156.
[17] R. Chmielowski, D. Pere, C. Bera, I. Opahle, W. Xie, S. Jacob, F. Capet, P. Roussel, A. Weidenkaff, G.K.H. Madsen, G. Dennler, J. Appl. Phys. 117 (2015) 125103.
[18] N.C. Miller, M. Bernechea, APL Mater. 6 (2018) 84503.
[19] H. Lin, Q. Zhu, D. Shu, D. Lin, J. Xu, X. Huang, W. Shi, X. Xi, J. Wang, L. Gao, Nat. Mater. 18 (2019) 602-607.
[20] J.P. Heremans, R.J. Cava, N. Samarth, Nat. Rev. Mater. 2 (2017) 1-21.
[21] M.Z. Mohyedin, M.F.M. Taib, A. Radzwan, M. Mustaffa, A. Shaari, O.H. Hassan, A.M.M. Ali, B.U. Haq, M.Z.A. Yahya, Mater. Renew. Sustain. Energy. 9 (2020) 3.
[22] Y. Min, G. Park, B. Kim, A. Giri, J. Zeng, J.W. Roh, S. Il Kim, K.H. Lee, U. Jeong, ACS Nano. 9 (2015) 6843-6853.
[23] Y. Xia, D. Qian, D. Hsieh, L. Wray, A. Pal, H. Lin, A. Bansil, D. Grauer, Y.S. Hor, R.J. Cava, M.Z. Hasan, Nat. Phys. 5 (2009) 398-402.
[24] G.R. Hyde, H.A. Beale, I.L. Spain, J.A. Woollam, J. Phys. Chem. Solids. 35 (1974) 1719-1728.
[25] P. Larson, V.A. Greanya, W.C. Tonjes, R. Liu, S.D. Mahanti, C.G. Olson, Phys. Rev. B 65 (2002) 1-11.
[26] Y.Y. Li, G. Wang, X.G. Zhu, M.H. Liu, C. Ye, X. Chen, Y.Y. Wang, K. He, L.L. Wang, X.C. Ma, H.J. Zhang, X. Dai, Z. Fang, X.C. Xie, Y. Liu, X.L. Qi, J.F. Jia, S.C. Zhang, Q.K. Xue, Adv. Mater. 22 (2010) 4002-4007.
[27] Y. Zhang, K. He, C.Z. Chang, C.L. Song, L.L. Wang, X. Chen, J.F. Jia, Z. Fang, X. Dai, W.Y. Shan, S.Q. Shen, Q. Niu, X.L. Qi, S.C. Zhang, X.C. Ma, Q.K. Xue, Nat. Phys. 6 (2010) 584-588.
[28] D. Hsieh, Y. Xia, D. Qian, L. Wray, F. Meier, J.H. Dil, J. Osterwalder, L. Patthey, A. V. Fedorov, H. Lin, A. Bansil, D. Grauer, Y.S. Hor, R.J. Cava, M.Z. Hasan, Phys. Rev. Lett. 103 (2009) 146401.
[29] A.O.M. Almayyali, B.B. Kadhim, H.R. Jappor, Phys. E Low-Dimensional Syst. Nanostructures. 118 (2020) 113866.
[30] M.M. Obeid, C. Stampfl, A. Bafekry, Z. Guan, H.R. Jappor, C. V. Nguyen, M. Naseri, D.M. Hoat, N.N. Hieu, A.E. Krauklis, T. V. Vu, D. Gogova, Phys. Chem. Chem. Phys. 22 (2020) 5354-15364.
[31] S.S. Abed Al-Abbas, M.K. Muhsin, H.R. Jappor, Superlattices Microstruct. 135 (2019) 106245.
[32] M.M. Obeid, M.M. Shukur, S.J. Edrees, R. Khenata, M.A. Ghebouli, S.A. Khandy, A. Bouhemadou, H.R. Jappor, X. Wang, Chem. Phys. 526 (2019) 110414.
[33] A. Bafekry, S.F. Shayesteh, F.M. Peeters, Phys. Chem. Chem. Phys. 21 (2019) 21070-21083.
[34] A. Bafekry, C. Stampfl, B. Akgenc, B. Mortazavi, M. Ghergherehchi, C. V. Nguyen, Phys. Chem. Chem. Phys. 22 (2020) 6418-6433.

[35] A. Bafekry, M. Yagmurcukardes, B. Akgenc, M. Ghergherehchi, C. V. Nguyen, J. Phys. D. Appl. Phys. 53 (2020) 355106.
[36] G. Cantele, D. Ninno, Phys. Rev. Mater. 1 (2017) 014002.
[37] A. Bafekry, C. Stampfl, F.M. Peeters, Phys. Status Solidi. 257 (2020) 2000182.
[38] D. Kong, K.J. Koski, J.J. Cha, S.S. Hong, Y. Cui, Nano Lett. 13 (2013) 632-636.
[39] C. Zhang, C. Zhang, H. Ng, Q. Xiong, Sci. China Mater. 62 (2019) 389-398.
[40] D.R. Kumar, T.T. Nguyen, C. Lamiel, J.J. Shim, Mater. Lett. 165 (2016) 257-262.
[41] M.Z. Xue, Z.W. Fu, J. Alloys Compd. 458 (2008) 351-356.
[42] G. Wang, X.G. Zhu, Y.Y. Sun, Y.Y. Li, T. Zhang, J. Wen, X. Chen, K. He, L.L. Wang, X.C. Ma, J.F. Jia, S.B. Zhang, Q.K. Xue, Adv. Mater. 23 (2011) 2929-2932.
[43] M.K. Jana, K. Biswas, C.N.R. Rao, Chem. - A Eur. J. 19 (2013) 9110-9113.
[44] D. Hsieh, D. Qian, L. Wray, Y. Xia, Y.S. Hor, R.J. Cava, M.Z. Hasan, Nat. 452 (2008) 970-974.
[45] Y. Yu, Z. Wu, O. Cojocaru-Miredin, B. Zhu, X.Y. Wang, N. Gao, Z.Y. Huang, F.Q. Zu, Sci. Rep. 7 (2017).
[46] R. Indirajith, M. Rajalakshmi, R. Gopalakrishnan, K. Ramamurthi, Superlattices Microstruct. 91 (2016) 165-172.
[47] F. Fei, Z. Wei, Q. Wang, P. Lu, S. Wang, Y. Qin, D. Pan, B. Zhao, X. Wang, J. Sun, X. Wang, P. Wang, J. Wan, J. Zhou, M. Han, F. Song, B. Wang, G. Wang, Nano Lett. 15 (2015) 5905-5911.
[48] P. Schonherr, S. Zhang, Y. Liu, P. Kusch, S. Reich, T. Giles, D. Daisenberger, D. Prabhakaran, Y. Chen, T. Hesjedal, Phys. Status Solidi - Rapid Res. Lett. 9 (2015) 130-135.
[49] N. Dhar, N. Syed, M. Mohiuddin, A. Jannat, A. Zavabeti, B.Y. Zhang, R.S. Datta, P. Atkin, N. Mahmood, D. Esrafilzadeh, T. Daeneke, K. Kalantar-Zadeh, ACS Appl. Mater. Interfaces. 10 (2018) 42603-42611.
[50] K.A. Messalea, A. Zavabeti, M. Mohiuddin, N. Syed, A. Jannat, P. Atkin, T. Ahmed, S. Walia, C.F. McConville, K. KalantarZadeh, N. Mahmood, K. Khoshmanesh, T. Daeneke, Adv. Mater. Interfaces. (2020) 2001131.
[51] J. P. Perdew, K. Burke, and M. Ernzerhof, Phys. Rev. Lett. 77 (1996) 3865 .
[52] J. P. Perdew, K. Burke, and M. Ernzerhof, Phys. Rev. Lett. 78 (1997) 1396 .
[53] G. Kresse and J. Hafner, Phys. Rev. B 47 (1993) 558 .
[54] G. Kresse and J. Hafner, Phys. Rev. B 49 (1994) 14251.
[55] J. Heyd, G. E. Scuseria, and M. Ernzerhof, J. Chem. Phys. 118 (2003) 8207.
[56] H.J. Monkhorst and J.D. Pack, Phys. Rev. B 13 (1976) 12.
[57] G. Henkelman, A. Arnaldsson, and H. Jonsson, Comput. Mater. Sci. 36 (2006) 354.
[58] S. J. Grimme, Comput. Chem. 27 (2006) 1787.
[59] D. Alfe, Comput. Phys. Commun. **180**, 2622 (2009).
[60] R. Hill, Proc. Phys. Soc., London, Sect. A 65 (1952) 349.
[61] H. Rojas-Chavez, H. Cruz-Martinez, E. Flores-Rojas, J.M. Juarez-Garcia, J.L. Gonzalez-Dominguez, N. Daneu, J. Santoyo-Salazar, Phys. Chem. Chem. Phys. 20 (2018) 27082.
[62] S. F. Pugh, Philos. Mag. 45, (1954) 823.
[63] W. C. Hu , Y. Liu , D. J. Li , X. Q. Zeng and C. S. Xu, Comput. Mater. Sci. 83, (2014) 27.